Received: 22 April 2021 | Revised: 9 June 2021 | Accepted: 14 June 2021

DOI: 10.1002/jbio.202100135

RESEARCH ARTICLE

JOURNAL OF BIOPHOTONICS

Modeling the efficiency of UV at 254 nm for disinfecting the different layers within N95 respirators

Abdallatif Satti Abdalrhman[1*] | Chengjin Wang[1] | Angelica Manalac[2] | Madrigal Weersink[2] | Abdul-Amir Yassine[3] | Vaughn Betz[3] | Benoit Barbeau[4] | Lothar Lilge[2,5] | Ron Hofmann[1]

[1]Department of Civil & Mineral Engineering, University of Toronto, Toronto, Ontario, Canada

[2]Department of Medical Biophysics, University of Toronto, Toronto, Ontario, Canada

[3]Department of Electrical & Computer Engineering, University of Toronto, Toronto, Ontario, Canada

[4]Department of Civil, Geological and Mining Engineering, Polytechnique, Montreal, Quebec, Canada

[5]Princess Margaret Cancer Centre, University Health Network, Toronto, Ontario, Canada

***Correspondence**
Abdallatif Satti Abdalrhman, Department of Civil & Mineral Engineering, University of Toronto, Toronto, ON (M5S 1A4), Canada.
Email: latif.abdalrhman@utoronto.ca

Abstract

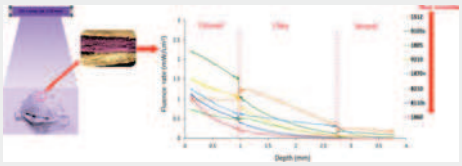

The study presented a Monte Carlo simulation of light transport in eight commonly used filtered facepiece respirators (FFRs) to assess the efficacy of UV at 254 nm for the inactivation of SARS-CoV-2. The results showed different fluence rates across the thickness of the eight different FFRs, implying that some FFR models may be more treatable than others, with the following order being (from most to least treatable): models 1512, 9105s, 1805, 9210, 1870+, 8210, 8110s and 1860, for single side illumination. The model predictions did not coincide well with some previously reported experimental data on virus inactivation when applied to FFR surfaces. The simulations predicted that FFRs should experience higher log reductions (>>6-log) than those observed experimentally (often limited to ~5-log). Possible explanations are virus shielding by aggregation or soiling, and a lack of the Monte Carlo simulations considering near-field scattering effects that can create small, localized regions of low UV photon probability on the surface of the fiber material. If the latter is the main cause in limiting practical UV viral decontamination, improvement might be achieved by exposing the FFR to UV isotropically from all directions, such as by varying the UV source to the FFR surface angle during treatment.

KEYWORDS

decontamination, filtering facepiece respirators, Monte Carlo, N95 reuse, SARS-CoV-2, UV

1 | INTRODUCTION

N95 filtering facepiece respirators (N95 FFRs) are an important barrier to COVID-19 infection, but they remain in short supply. The application of ultraviolet (UV) light at 254 nm (UV_{254}) to decontaminate and reuse the FFRs is helping to alleviate the crisis, but the process is still not fully understood [1]. The effectiveness is dependent on the application of a sufficient UV dose to inactivate the targeted pathogens. The UV "dose" properly refers to the UV fluence (mJ/cm^2) reaching the pathogens of interest and not the surface radiant exposure (mJ/cm^2) provided by the UV source. This is critical considering that the targeted organisms in many cases could be embedded within the material and/or covered within saliva, as the case for an N95 FFR. Therefore, the

properties of the material being disinfected will influence the UV light fluence distribution as a function of depth into the material. Materials allowing pathogens to be embedded within and thereby partially or fully shielded from the UV radiation will be more challenging to disinfect than those on a flat surface that leave the pathogens directly exposed to the incoming photon radiant exposure.

Previous studies of the effectiveness of UV to decontaminate FFRs are summarized in Table 1. In general, the organisms were placed on the surface of the FFR or were otherwise not actively inserted within the depth of the material. The organisms tested included H1N1/H5N1 virus, *Bacillus subtilis* endospores and MS2 coliphage. The maximum UV radiant exposures at the outer surface of the FFRs were in the order of 1000 to 7000 mJ/cm^2 and achieved up to 4 to 5 log inactivation of the targeted organisms, which in most cases was close to the maximum reported inactivation level. Some recent studies have also demonstrated the effectiveness of UV_{254} for decontaminating N95 FFRs inoculated with SARS-CoV-2 virus [2, 3]. Geldert et al showed that a surface UV_{254} radiant exposure of 50 mJ/cm^2 was required to achieve 3 log reduction for SARS-CoV-2 virus (applied as liquid droplets on the FFR's surface), while applying 500 mJ/cm^2 resulted in >5 log reduction [3]. Ozog et al showed that a UV_{254} radiant exposure of 1500 mJ/cm^2 on each side of different N95 FFR models inoculated with SARS-CoV-2 virus resulted in complete observable decontamination (>4 log reduction) [2].

A gap in the research to date on UV_{254} treatment for N95 FFR decontamination is the potential for viruses to penetrate the FFR such that its material may partially shield the pathogens from UV exposure. Most N95 FFRs contain three main layers of polymeric fabrics (such as polypropylene and polyester) and cellulose nonwoven fabrics [4–6]. Generally, the inner and outer layers provide form, stability, comfort, water resistance and large particle filtration. The filtration (middle) layer acts as the principal trapping media for submicron particles. The filtration layer comprises polypropylene microfibers with a diameter in the range from ~1 to 10 μm arranged as a three-dimensional network [4–6]. Considering the small fiber diameters, the void space within this layer is usually vast. This will make the filtration efficiencies of melt-blown fabrics by themselves very low for trapping fine particles through size exclusion. To improve the filtration efficiency while keeping the same high air permeability, these fibers are charged through corona discharge and/or triboelectric means to improve electrostatic particle trapping properties [4].

The importance of embedded viruses to infection risk is still unknown. It has been argued that embedded viruses, especially those electrostatically attracted to the inner filter layer, are largely immobile during breathing [7]. While the release of MS2 viruses from contaminated FFRs was shown to be low [7], risk assessment needs to be updated for new viruses such as the SARS-CoV-2. More importantly, evidence to support the complete absence of release during handling or donning and doffing is unknown to the authors. As such, it is arguably prudent to assume that any virus trapped within an FFR represents a continuing risk of infection and should be targeted during decontamination. While exploring the ability of UV to inactivate viruses embedded within the depths of an FFR would ideally involve empirical testing, such work is highly challenging and time-consuming. In the meantime, this article describes mathematical modeling to predict the ability of UV_{254} to penetrate different N95 FFRs to inactivate embedded SARS-CoV-2 virus on a mesoscopic length scale based on the optical properties of the material layers of eight common FFRs recently reported by Lilge et al [6]. While such model predictions based on assumptions are no replacement for experiments, the results can guide decontamination practices in the absence of better empirical data as the world tries to cope with the COVID-19 pandemic under very challenging circumstances.

2 | MATERIALS AND METHODS

2.1 | FFRs optical properties

The eight FFRs used in this simulation study are 3 M models 1805, 9105s 1860, 8110s, 8210, 1870+, 9210 and Moldex model 1512. The optical properties of each of the three layers of the FFRs at 254 nm were obtained from the study by Lilge et al [6]. In brief, the previous work calculated the optical properties of fabric layers at four wavelengths between 250 and 300 nm, based on the transmission and reflection spectra of the fabric layer materials and assumed refractive indices based on the refractive index of fabric fibers and average densities of fabrics. Only far field, transmission and reflection measurements were feasible, limiting the extraction of the optical interaction coefficients to the absorption and reduced light scattering coefficients of the FFR fabrics. Measurements were performed on non-compressed fabric layers. The macroscopic optical properties for the complete fabric layer were derived based on the IAD code developed by Prahl et al [15] and used for the current simulations pertaining to UV_{254}. The fabric optical properties of the different FFRs at 254 nm are summarized in Table 2.

TABLE 1 Application of UV_{254} for the decontamination of N95 FFRs

Publication	Organisms	FFR type	Method to load the virus	Soiling agents	UV radiant exposure (mJ/cm^2)	Log reduction
Heimbuch and Harnish [8]	H1N1	15 models	Intact FFRs were inoculated with 10 1-μL droplets of virus (10^9 $TCID_{50}$/mL) on 4 different locations	Mucin	1000	1.42-4.79
				Sebum		1.25-4.64
Mills et al [9]	H1N1	15 models	Intact FFRs were inoculated with 10 1-μL droplets of virus (10^7) within a 2 cm^2 area	Mucin	1100	1.42-4.79
				Sebum		1.25-4.49
Lin et al [10]	*Bacillus subtilis* spores	3 M 8210	Nebulizer + suction	None	1100	~2.2
					2200	~2.8
					5700	No viable virus
Woo et al [11]	MS2	3 M 1870	Nebulizer + suction	None	900	3.4
				None	1800	4.4
				beef extract		1.3
				artificial saliva		1.5
				None	3600	5
				beef extract		2.3
				Artificial saliva		2.7
				beef extract	7200	2.5
				Artificial saliva		3.6
Fisher and Shaffer [12]	MS2	6 models	Nebulizer + suction	None	1000 (at the internal layer)	3
Lore et al [13]	H5N1	3 M 1860 and 1870	Nebulizer, no suction	None	1800	≥4.5; No viable virus
Vo et al [14]	MS2	Wilson N1105	Nebulizer, no suction	None	1440	1.83
					2880	2.64
					4320	3.00
					5760	3.16
					7200	No viable virus

TABLE 2 Fabric optical properties of the eight FFRs at 254 nm

Model	Outer layer (L1)			Filter (L2)			Inner layer (L3)		
	μ_a (mm^{-1})	μ_s'	μ_{eff}	μ_a (mm^{-1})	μ_s'	μ_{eff}	μ_a (mm^{-1})	μ_s'	μ_{eff}
1805	0.539	0.494	0.656	0.178	2.387	0.476	0.355	0.278	0.324
8110 s	0.378	1.758	0.867	0.329	3.389	1.049	1.185	4.919	4.552
1860	0.571	2.870	1.674	0.248	3.145	0.762	0.891	4.096	3.123
1870+	0.245	1.641	0.543	0.38	1.706	1.542	0.819	6.283	3.555
8210	0.386	1.926	0.928	0.222	3.116	0.679	0.894	4.187	3.167
9105 s	0.005	1.930	0.012	0.193	1.835	0.453	0.001	1.920	0.002
9210	0.144	1.327	0.287	0.223	2.950	0.663	0.361	2.206	0.929
1512	0.044	0.004	0.005	0.342	1.93	0.823	0.001	3.248	1.109

Note: μ_a: Absorption coefficient (mm^{-1}). μ_s': Reduced scattering coefficient (mm^{-1}). $\mu_{eff} = \sqrt{3\mu_a(\mu_a + \mu_s')}$ Effective attenuation coefficient (mm^{-1}).

2.2 | Monte Carlo-based UV fluence rate distribution within FFRs

To estimate the UV fluence rate (mW/cm^2) at 254 nm at any point across the FFR depth (Figure 2), Monte Carlo (MC)-based photon propagation simulations [16] were performed. While the fabrics comprise micron-sized fibers with varying degrees of packing densities and orientations, light propagation simulations, such as FullMonte, assume bulk optical properties and light propagation based on the radiation transport theory. For FullMonte simulations, the measured reduced scattering coefficient was split into the scattering coefficient with an assumed anisotropy factor of 0.9 so that $\mu_s' = \mu_s(1 - g)$ is satisfied. During simulations, the Henyey-Greenstein phase function was applied. The light source was modeled as a flat disc of 12 cm diameter and centered parallel at 10 cm over a 24-cm-diameter flat three-layered disc representing the FFR. Photons are emitted randomly from the source surface, either normal to the surface or within a user-defined solid angle, to simulate the source's emission properties using FullMonte [17]. A total of 10^8 photon packets were launched in each FullMonte simulation. For depth profiles, only fluence rate data from the central 10-cm-diameter disc of the FFR disc were used to avoid any simulations boundary effects. More details can be found in the study by Lilge et al [6]. Simulations were executed with micron-sized tetrahedral voxels, and then, the photon weight per voxel volume was converted into fluence-rate values, which resulted in rounding error causing noise; hence, a boxcar smoothing algorithm was applied.

To validate the measurements (see Section 3.1), the mesoscopic light transmission properties of four mask models were also measured using a radiometer (IL400A, International Light, USA). The four models were separated into their three main fabric layers: L1 (external), L2 (filter) and L3 (inner); the filter layer in models 1870+ and 1512 were separated into two layers: L2 and L2*. The layers were then placed over the UV sensor and irradiated with 128 mJ/cm^2 over 90 seconds. The UV irradiance reaching the UV sensor was used to calculate the transmittance of the layer (UVT [%] measured fluence/applied fluence × 100). All measurements were taken in duplicate. The average coefficient of variations amongst replicates was 8.8% (Table 3).

TABLE 3 UV transmittance at 254 nm of four FFRs by radiometer

Models	UVT (%) per layer			
	L1	L2	L2*	L3
8210-A	7.0	16.2		0.22
8210-B	8.4	18.7		0.23
AVG	**7.7**	**17.4**		**0.23**
1860-A	4.3	14.4		0.46
1860-B	6.1	17.0		0.38
AVG	**5.2**	**15.7**		**0.42**
1870 + -A	30	41	0.50	48
1870 + -B	31	41	0.51	56
AVG	**30**	**41**	**0.50**	**52**
1512-A	25	38	43	21
1512-B	30	43	45	25
AVG	**28**	**40**	**44**	**23**

To calculate the log inactivation, a homogenous viral contamination across the FFR depth was assumed, and

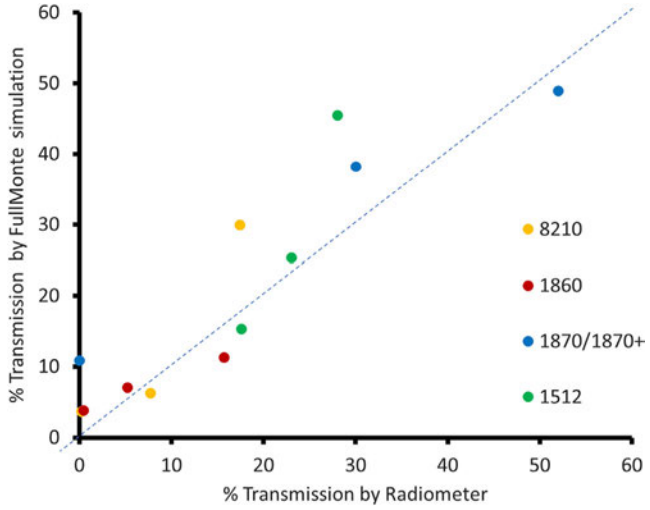

FIGURE 1 Comparison of UV_{254} light transmission through the three layers in 8210, 1860, 1870/1870+ and 1512 FFRs. The standard error for the radiometer transmission measurements is 5.6% at the highest (for high transmission in the 1870/1870+ model) and generally <2% (n = 2). The standard deviation for FullMonte simulation results is negligible. The line of identity is indicated by the dashed line

the inactivation probability at each depth was calculated based on the simulated fluence rates at that depth and then summed across all depths. Homogenous viral contamination across the FFR depth was assumed as a conservative scenario where viruses could go deeply inside the mask as opposed to accumulating solely near the surface.

3 | RESULTS AND DISCUSSIONS

3.1 | Fluence rate distribution as a function of FFR depth

Figure 1 compares the UV_{254} transmission (%) through FFR layers based on the radiometric method and transmission simulations based on MC methods for models 8210, 1860, 1870+ and 1512. While the transmission for the layers is slightly higher for the FullMonte simulations, the two techniques have shown an overall good correlation across the multiple fabric layers (slope = 0.97, only three datapoints deviated by more than 10% but still less than 15%), suggesting that the derived optical properties and fluence-rate gradients are reasonable predictions of the macroscopic UV_{254} fluence distribution in the evaluated FFRs. It is noteworthy that the radiometry and FullMonte simulations are based on the radiation transport theory, which assumes independent scattering events.

The fluence rate quantifies the omnidirectional power density in turbid media as mW/cm^2 and conceptually represents the UV radiation intensity at that point. In this work, only 254 nm UV radiation is modeled, representing a low-pressure mercury lamp. In Figure 2, the predicted fluence rate is shown as a function of depth for the eight N95 FFRs, assuming an irradiance of 1 mW/cm^2 applied only on the outer surface of the FFR (Figure 2A) or applying 1 mW/cm^2 to both inner and outer surfaces of the FFR (Figure 2B). To obtain a radiant exposure of 1000 mJ/cm^2 at the FFR surface, a common reported energy density in previous research, an exposure time of 1000 seconds would be required (about 17 minutes). It becomes apparent from Figure 2 that the reported fluence rate inside the FFR and proximal to the surface (e.g., at 0.1 mm depth) can be higher than the surface irradiance. While the higher photon density or brightness inside the FFR may seem counterintuitive, this is a normal phenomenon caused by backscattering inside high albedo materials, leading to a higher steady-state photon concentration in that region. It is evident from Figure 2 that some of the FFRs have higher albedo than others, resulting in a predicted higher fluence rate within these FFRs' deeper layers. This is desirable for the decontamination of the FFRs. Unfortunately, without full knowledge of the exact FFR materials and construction, we cannot propose the specific material properties that enhance the backscattering. For now, our conclusions must remain entirely observational. Some types of N95 FFRs permit higher UV fluences throughout their layers for the same applied surface irradiance attributable to the higher scattering coefficients, theoretically resulting in higher decontamination efficiency using UV_{254}.

A second observation from Figure 2 is that the fluence rate decreases significantly between the outer surface being exposed to UV and the inner filter layer, where presumably many viruses might be trapped. This brings into question whether the disinfection of the FFRs would be practical if we are concerned about viruses that may be attached to that inner filter layer. More about this is discussed in the next section. The discontinuity in the UV fluence between each of the three layers is due to the backscattering effect, previously described, at material interfaces.

A third observation is that the fluence rate within the FFR is much higher if exposed from both directions (inner and outer). While this is intuitively obvious, the data in Figure 2 suggest that there can be a significant improvement to the UV fluence delivered to the inner filter layer by exposing the FFRs from both sides, especially for those FFRs that are most transmissive to the UV. When exposing the FFRs from both sides, some of the FFRs can exhibit a fluence rate in the inner layer that is as much as half of the irradiance at the outer surface.

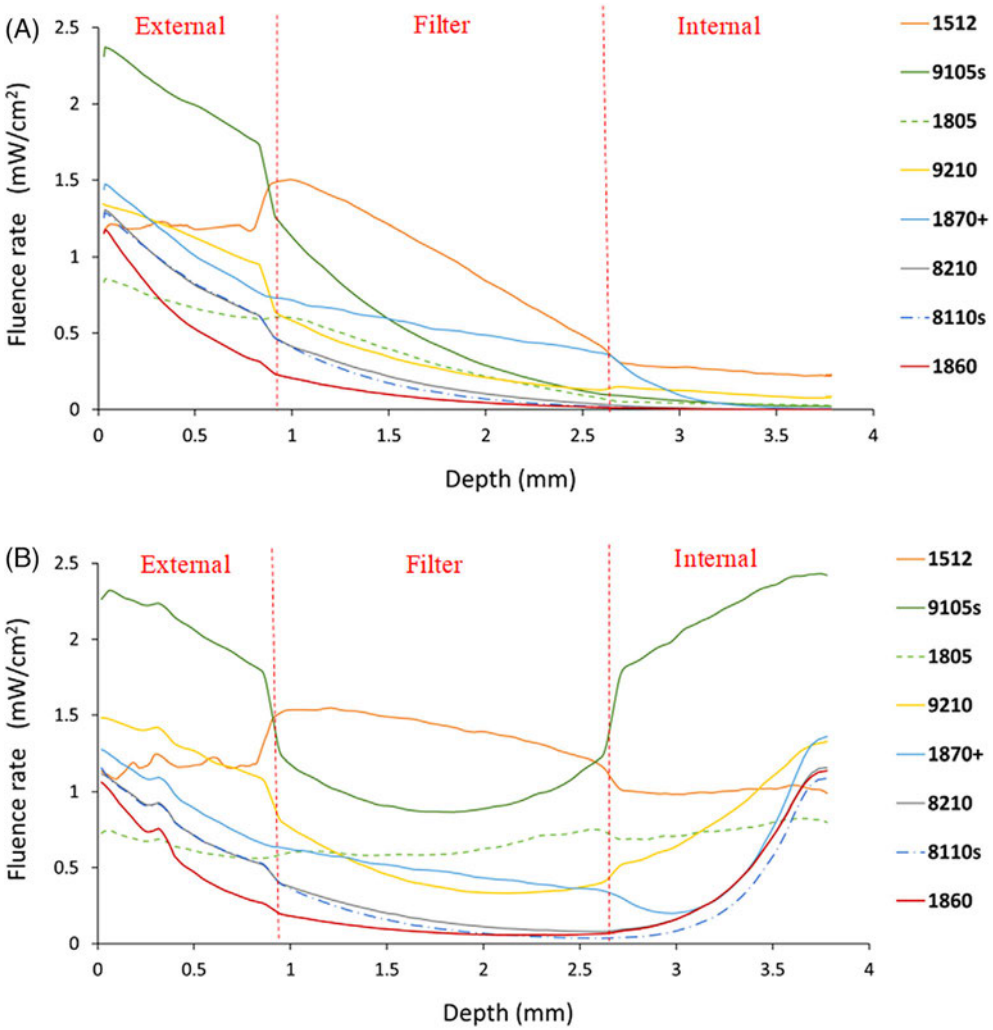

FIGURE 2 Simulation of the fluence rate with depth within the three layers of different N95 FFRs models: A, UV irradiation from one side (1 mW/cm^2); B, UV irradiation from two sides (1 mW/cm^2 on each side)

3.2 | Simulation of SARS-CoV-2 inactivation at different depths and on separate layers

To understand the efficiency of UV_{254} for the inactivation of SARS-CoV-2 at different depths within the FFRs, the UV_{254} fluence rate predictions from Figure 2 were converted into fluences for different surface irradiances. While the UV fluence response of SARS-CoV-2 is still uncertain, the available data so far agree well with other single-stranded ribonucleic acid (ssRNA) viruses for which such information is well established [18, 19]. In our model, we have used the most conservative fluence response data from Patterson et al [20], reporting a fluence-per-log of 5.3 mJ/cm^2 for UV_{254}. Other studies reported or predicted SARS-CoV-2 fluence-per-log data between 1.2 and 2.5 mJ/cm^2 [18, 21, 22]. We used our model to predict the log inactivation of SARS-CoV-2 at different depths in the eight FFRs for a single UV_{254} surface irradiance of 100 mJ/cm^2 (Figure 3A) or illumination of both sides with an irradiance of 50 mJ/cm^2 (Figure 3B).

To obtain the results shown in Figure 3, it was assumed that the viruses were homogenously distributed throughout the FFR depth. The resulting inactivation performance within the FFRs varied with depth and differed between models. When 100 mJ/cm^2 UV_{254} radiant exposure was applied only on the outer FFR layer (Figure 3A), viral inactivation was very high proximal to the surface (>10^{14}). Still, it showed a strong depth gradient dipping until it reached <5 log inactivation on the inside of the FFR (four FFR models recorded 0 log inactivation at a particular depth). On the other hand, when the same total radiant exposure (100 mJ/cm^2) was applied from both sides (50 mJ/cm^2 each) (Figure 3B), the inactivation performance within the FFRs was greatly enhanced. Two models (1512 and 9105s) maintained >9 log inactivation across the whole FFR thickness, and there were no 0 log inactivation points within any of the studied models. This again emphasizes the benefits of applying UV from both sides of the N95. This can be achieved in practical applications by having two UV light sources, one on each side, or by rotating the FFRs half-

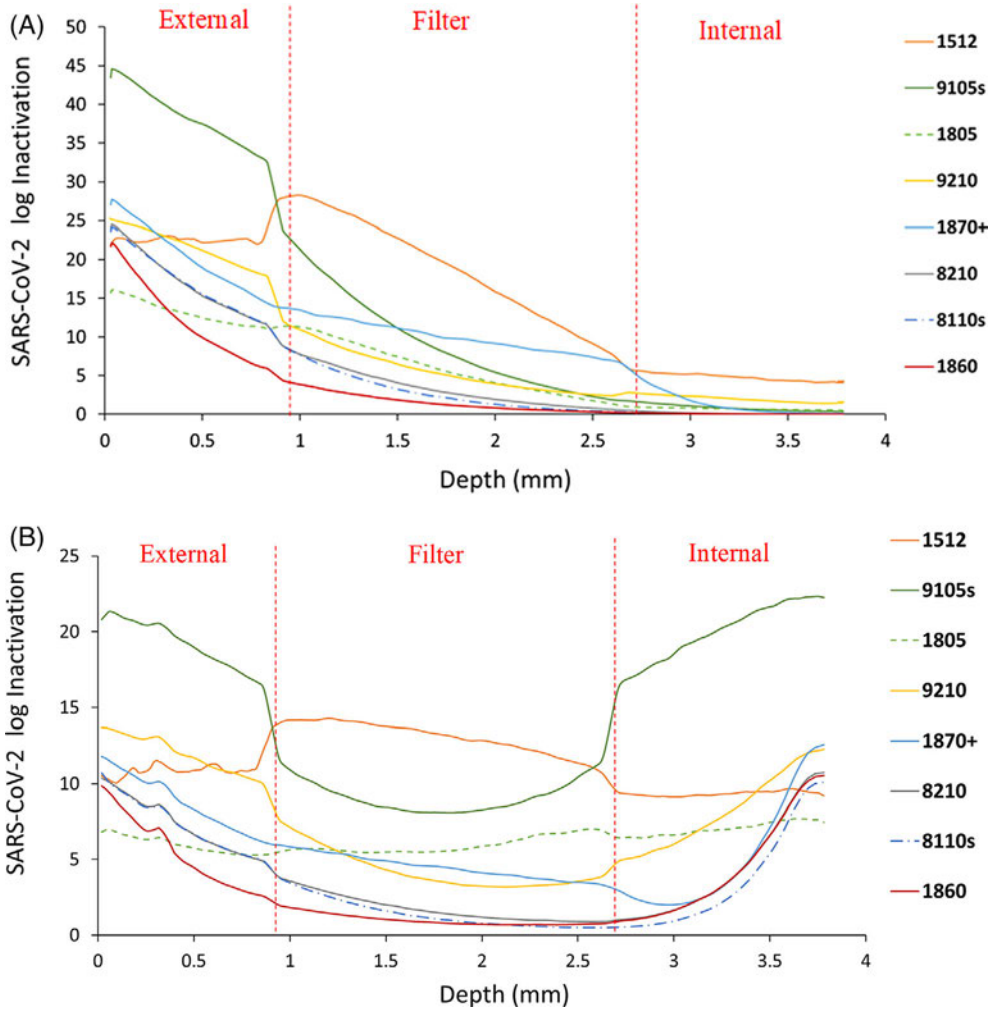

FIGURE 3 Simulation of the SARS-CoV-2 inactivation at different depths and layers within different N95 FFRs models using UV_{254}: A, UV irradiation from one side (1 mW/cm^2 for 100 seconds = 100 mJ/cm^2 total fluence) and B, UV irradiation from two sides (1 mW/cm^2 on each side for 50 seconds = 50 mJ/cm^2 fluence on each side)

way through the decontamination if the light source is on only one side.

The total SARS-CoV-2 log inactivation for each layer within the FFRs was estimated (Figure 4). As shown in Figures 3 and 4, for identical UV irradiance, there was a clear difference in terms of inactivation performance between the different FFR models. For instance, models 1512 and 9105s showed relatively better and more homogenous inactivation performances across the different layers when compared to other models. These two FFR models have the lowest effective light attenuations, given by $\mu_{\text{eff}} = \sqrt{3\mu_a(\mu_a + \mu_s')}$, across all layers (Table 2).

3.3 | Comparison of UV_{254} light propagation simulation and inactivation experiments, and their limitations

We can compare the theoretically attainable SARS-Cov-2 log inactivation predicted by our model (Figure 4) with those obtained experimentally by Geldert et al [3], with the caveat that we assumed homogenous virus distribution, which is not given in the experimental studies. In experiments, Geldert et al [3] reported achieving 3 log inactivation for a 3 M 1860 N95 FFR model inoculated using 50 μL liquid drops of SARS-CoV-2 stock when a UV_{254} surface radiant exposure of 50 mJ/cm^2 was applied [3]. Our simulation model predicted that at the same dose, the inactivation at the external layer (where, based on their application method, the majority of the applied virus would presumably be located) would be 5.8 log, whereas the inactivation at the middle layer (where some of the applied virus might be located) would be 0.9 log (Figure 4A). Geldert et al also reported >5 log inactivation for a radiant exposure of 500 mJ/cm^2, where the model predicted achieving >20 log inactivation (total log inactivation) for the external layer and 2.4 log inactivation for the middle layer (Figure 4B). In another study, Ozg et al [2] showed that a 1500 mJ/cm^2 surface radiant exposure to both FFRs sides led to >4 log inactivation (total log inactivation) for different N95 FFRs models (3 M 1860, 8210, 8511, 9211; Moldex 1511). Our model predicts that a surface radiant exposure of 1500 mJ/cm^2 on both sides yields >20 log inactivation (total log

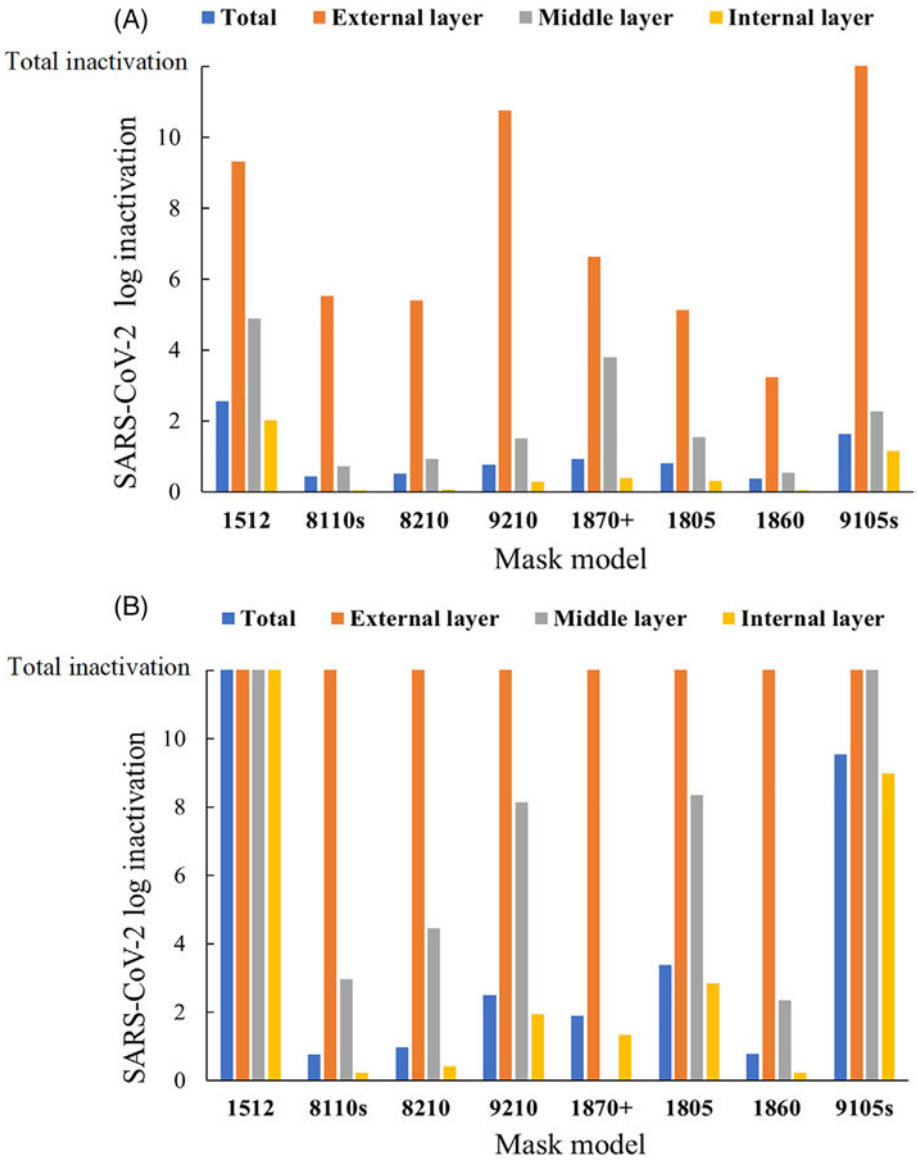

FIGURE 4 Total modeled SARS-CoV-2 inactivation for each layer within different N95 FFRs models using UV_{254} irradiation from one side at radiant exposures of, A, 50 mJ/cm^2 at the surface and, B, 500 mJ/cm^2 at the surface

inactivation) at the external layer and >11 log inactivation on the filter layer for all models.

There is a greater disagreement between our model simulations and earlier studies using other viruses, as shown in Table 1. The viruses tested in Table 1 exhibit relatively similar sensitivities to UV_{254} as our modeled SARS-CoV-2, with the fluence-per-log for these viruses often in the range of 4 to 35 mJ/cm^2/log [23–25]. As such, the predicted high SARS-CoV-2 inactivation at the FFR surfaces shown in Figure 3 (typically 10-40 log) implies that there should be similarly high inactivation rates for these other viruses assuming that these previous studies measured the inactivation of viruses near the surface of the FFR fabrics. Instead, the experiments reported in Table 1 showed that UV radiant exposures in the order of 1000 to 2000 mJ/cm^2 often led to log reductions in the 3 to 5 range. There are several possible explanations for this that mainly concern the concept of a UV dose distribution and tailing. In UV disinfection, not all organisms receive the same UV dose: Some organisms may be shielded from UV exposure due to being embedded within an opaque particle or within an aggregation of viruses, or are protected by being lodged in a crevice of the material, etc. The maximum log inactivation attainable in a UV disinfection system is governed by the number of the organisms in these low-dose regions. For example, if there are 10 000 viruses in a system and 1 is completely shielded from UV light, then the maximum log inactivation that can ever be achieved, even with an infinitely powerful UV light source, is 4 log (i.e., 1 survivor given 10 000 initial organisms). It is possible that the relatively low log inactivation reported in Table 1 given the high UV fluences of >1000 mJ/cm^2 is a reflection of this tailing in the UV dose distribution. The tailing could be caused by several factors.

One such factor relates to far-field and near-field scattering domains, with the near-field creating small and localized destructive interference or "shadowed" regions. Radiometry measures and Monte Carlo simulates the photon density based on the radiative transport equation, which is valid only in the scattering far field. For the fiber materials in the FFRs with a diameter D of 1.2 μm, the scattering far field is given by $2\frac{D^2}{\lambda}$ ~11 μm comparable with the inter fiber distance of 4 to 5 μm based on the mean flow pore diameter of the filter materials. However, trapped viruses are located on the surface of these fibers and hence in the scattering near-field domain given by $R < 0.62\sqrt{\frac{D^3}{\lambda}}$, equivalent to ~1.6 μm for the above conditions. Schaefer et al presented approaches to calculating the spatial electric field distributions in the near field based on an analytical solution of the wave equation and a numerical finite difference time domain method for coherent and collimated light sources [26]. Both approaches showed that the electric field on the immediate surface of a dielectric cylinder, particularly in the direction of light propagation, can result in spots large enough to contain viruses (in areas where the electric fields cancel out, and the photon density is zero). While experimental results were obtained by noncoherent and non-collimated light sources, the large source to FFR distance implies that the photons enter the fabric only from a small solid angle, reducing the electric field heterogeneities around the fabric fibers so not eliminating it. In other words, the viruses may be lodged in small regions that are void or very restricted in UV irradiance due to the near-field scattering effects. Hence, simulating the fluence distribution in FFRs based on scattering far-field approximations, as was performed in this study, might be insufficient to predict the UV decontamination reality. They cannot capture the minute spatial detail to predict the fluence distribution at the required spatial resolution accurately. Analytical solutions or finite difference time domain calculations require significant computational power, particularly in memory, to be implemented on a physical scale necessary for modeling FFRs [27]. However, the analytical solution of the wave equation determining the electric field intensity, and hence the probability of the photon presence on the surface of realistic FFR material sections, for parallel and wide-angle incidence could determine the prevalence of low photon locations comparable to the size of viruses. Performing these calculations is beyond the aim of the current study but should be executed in the future to determine the fabric fiber surface area fraction receiving low UVC fluence.

This issue of submicron low-irradiance regions in the FFR due to near-field scattering effects could potentially be avoided by applying UV to the FFR while changing the angle between the incoming UV irradiation and the FFR, or by ensuring that the UV source is irradiating the FFR from all directions. Experiments could be conducted to compare the log reduction of applied viruses when the UV is applied from mostly one direction versus a multidirectional system.

Another factor that might lead to the lower effectiveness of UV decontamination in practice compared with the simulation reported in this study is soiling of the viruses. The fluence-per-log used in this simulation was 5.3 mJ/cm^2, similar to many viruses when tested in a pure culture. Viruses in the environment, however, may be soiled with the material that can inhibit the passage of UV photons. Baranchesme et al recently reported that salts and other materials in saliva and mucus are quite opaque to UV photons at 254 nm [28]. For example, the UV absorbance of human saliva (N = 18) was reported to be 6.2 cm^{-1} (min-max: 2.4-13.1). Microbes that are partially shielded by such material will therefore experience a reduced log inactivation compared with that predicted in the simulations of this study. The UV_{254} inactivation of *B. subtilis* spores dried in human saliva on a glass surface plateaued at 2.5 to 3.0 log inactivation for fluences above 100 mJ/cm^2. The formation of aggregates during drying is expected to cause this deviation from the linearity of the dose-response curve. Therefore, the model could be improved by using a dose-response curve, which accounts for the interference from soiling. The aggregation of viruses itself can also modify the local optical properties within the context suggested above, and a careful investigation of this is needed in the future.

Finally, while this study was performed only for 254 nm, the general finding would apply to the entire UVC region. Longer wavelengths may be less impacted by saliva and light scattering will be reduced as anticipated for Mie scattering according to the $1/\lambda$ relationship. Conversely, shorter wavelengths including 222 nm, now being investigated for air and surface sterilization due to being potentially safe for the skin and eye exposure [29], will experience higher light scattering and absorption by the fabric fibers as well as saliva, making it less suitable for sterilization for turbid media.

4 | CONCLUSION

This study presented a simulation to assess the efficacy of UV at 254 nm for the inactivation of SARS-CoV-2 at different depths and fabric layers in eight different FFR models. Certain FFRs were predicted to be inherently more treatable using UV_{254}. The different eight FFRs models used in this study can be classified into three groups based on their suitability for UV_{254} decontamination: models 1512 and 9105s (theoretically easy to decontaminate); models 1805, 9210 and 1870+ (theoretically

moderate to decontaminate); and models 8210, 81 102 and 1860 (theoretically more difficult to decontaminate). Our model did not coincide well with some of the previously reported experimental data about virus inactivation. In particular, our model predicted that FFRs are more easily decontaminated than those reported previously. One explanation may be that there is a submicron UV dose distribution heterogeneity around the FFR fibers that our macroscopic simulation model does not adequately capture. In addition, microorganisms may experience shielding from the UV radiation by either aggregation, by being soiled, or due to near-field scattering effects that can create small, localized regions of low UV photon probability within the fiber material. The near-field scattering effects may potentially be overcome by exposing the material to light from different directions during decontamination, such as by rotating either the light or the FFR during treatment, or by using a static system whereby the UV light is delivered from multiple directions.

CONFLICT OF INTEREST

The authors declare no financial or commercial conflict of interest.

AUTHOR BIOGRAPHIES

Please see Supporting Information online.

DATA AVAILABILITY STATEMENT

All data will be placed on a publicly accessible server for review and use by the scientific community.

ORCID

Abdallatif Satti Abdalrhman https://orcid.org/0000-0002-8161-3815
Lothar Lilge https://orcid.org/0000-0001-5533-0005

REFERENCES

[1] R. J. Fischer, D. H. Morris, N. van Doremalen, S. Sarchette, M. J. Matson, T. Bushmaker, C. K. Yinda, S. N. Seifert, A. Gamble, B. N. Williamson, S. D. Judson, E. de Wit, J. O. Lloyd-Smith, V. J. Munster, *Emerg. Infect Dis.* **2020**, *26*, 2253.
[2] D. M. Ozog, J. Z. Sexton, S. Narla, C. D. Pretto-Kernahan, C. Mirabelli, H. W. Lim, I. H. Hamzavi, R. J. Tibbetts, Q.-S. Mi, *Int. J. Infect. Dis.* **2020**, *100*, 224.
[3] A. Geldert, A. Su, A. W. Roberts, G. Golovkine, S. M. Grist, S. A. Stanley, A. E. Herr, *medRxiv* **2021**.
[4] L. W. Barrett, A. D. Rousseau, *Am. Ind. Hyg. Assoc. J.* **1998**, *59*, 532.
[5] L. Liao, W. Xiao, M. Zhao, X. Yu, H. Wang, Q. Wang, S. Chu, Y. Cui, *ACS Nano* **2020**, *14*, 6348.
[6] L. Lilge, A. Manalac, M. Weersink, F. Schwiegelshohn, T. Young-Schultz, A. S. Abdalrhman, C. Wang, A. Ngan, F. X. Gu, V. Betz, *J. Biophoton.* **2020**, *13*(12), e202000232.
[7] E. M. Fisher, A. W. Richardson, S. D. Harpest, K. C. Hofacre, R. E. Shaffer, *Ann. Occup. Hyg.* **2012**, *56*, 315.
[8] B. Heimbuch, D. Harnish, *Appl. Res. Assoc.* **2019**, 275.
[9] D. Mills, D. A. Harnish, C. Lawrence, M. Sandoval-Powers, B. K. Heimbuch, *Am. J. Infect. Control* **2018**, *46*, e49.
[10] T. H. Lin, F. C. Tang, P. C. Hung, Z. C. Hua, C. Y. Lai, *Indoor Air* **2018**, *28*, 754.
[11] M.-H. Woo, A. Grippin, D. Anwar, T. Smith, C.-Y. Wu, J. D. Wander, *Appl. Environ. Microbiol.* **2012**, *78*, 5781.
[12] E. M. Fisher, R. E. Shaffer, *J. Appl. Microbiol.* **2011**, *110*, 287.
[13] M. B. Lore, B. K. Heimbuch, T. L. Brown, J. D. Wander, S. H. Hinrichs, *Ann. Occup. Hyg.* **2012**, *56*, 92.
[14] E. Vo, S. Rengasamy, R. Shaffer, *Appl. Environ. Microbiol.* **2009**, *75*, 7303.
[15] S. A. Prahl, M. J. van Gemert, A. J. Welch, *Appl. Opt.* **1993**, *32*, 559.
[16] J. Cassidy, A. Nouri, V. Betz, L. Lilge, *J. Biomed. Opt.* **2018**, *23*, 085001.
[17] T. Young-Schultz, S. Brown, L. Lilge, V. Betz, *Biomed. Opt. Express* **2019**, *10*, 4711.
[18] N. C. Rockey, K. Chin, J. B. Henderson, L. Raskin, K. Wigginton, *bioRxiv* **2020**, *55*(5), 3322.
[19] C.-C. Tseng, C.-S. Li, *J. Occup. Environ. Hyg.* **2007**, *4*, 400.
[20] E. I. Patterson, T. Prince, E. R. Anderson, A. Casas-Sanchez, S. L. Smith, C. Cansado-Utrilla, T. Solomon, M. J. Griffiths, Á. Acosta-Serrano, L. Turtle, *J. Infect. Dis.* **2020**, *222*, 1462.
[21] N. Storm, L. G. McKay, S. N. Downs, R. I. Johnson, D. Birru, M. de Samber, W. Willaert, G. Cennini, A. Griffiths, *Sci. Rep.* **2020**, *10*, 1.
[22] B. Pendyala, A. Patras, B. Pokharel, D. D'Souza, *Front. Microbiol.* **2020**, 11. https://doi.org/10.3389/fmicb.2020.572331
[23] G. Chevrefils, É. Caron, H. Wright, G. Sakamoto, P. Payment, B. Barbeau, B. Cairns, *IUVA News* **2006**, *8*, 38.
[24] A. H. Malayeri, M. Mohseni, B. Cairns, J. R. Bolton, G. Chevrefils, E. Caron, B. Barbeau, H. Wright, K. G. Linden, *IUVA News* **2016**, *18*, 4.
[25] J. J. McDevitt, S. N. Rudnick, L. J. Radonovich, *Appl. Environ. Microbiol.* **2012**, *78*, 1666.
[26] J. Schaefer, S.-C. Lee, A. Kienle, *J. Quant. Spectrosc. Radiat. Transf.* **2012**, *113*, 2113.
[27] F. Ott, B. Krüger, A. Liemert, A. Kienle, *J. Quant. Spectrosc. Radiat. Transf.* **2019**, *235*, 40.
[28] F. Barancheshme, J. Philibert, N. Noam-Amar, Y. Gerchman, B. Barbeau, *J. Photochem. Photobiol. B: Biol.* **2021**, *217*, 112168.
[29] *J. Cadet. Photochem. Photobiol.* **2020**, *96*, 949.

SUPPORTING INFORMATION

Additional supporting information may be found online in the Supporting Information section at the end of this article.

How to cite this article: A. S. Abdalrhman, C. Wang, A. Manalac, M. Weersink, A.-A. Yassine, V. Betz, B. Barbeau, L. Lilge, R. Hofmann, *J. Biophotonics* **2021**, *14*(10), e202100135. https://doi.org/10.1002/jbio.202100135